Unveiling the electronic structure of the predicted topological superconductor $PbTaS_2$

Wenjuan Zhao,[1,*] Jingjing Gao,[2] Xin Liang,[2] Giovanni Di Santo,[1] Chunyao Song,[3] Wenjian Lu,[2,†] Xuan Luo,[2] Yuping Sun,[2,4,5] Guodong Liu,[6] and Luca Petaccia[1,‡]

[1]*Elettra Sincrotrone Trieste, Strada Statale 14 km 163.5, 34149 Trieste, Italy*

[2]*Key Laboratory of Materials Physics, Institute of Solid State Physics, HFIPS, Chinese Academy of Sciences, Hefei 230031, People's Republic of China*

[3]*Beijing Orient Institute of Measurement and Test, Beijing 100086, People's Republic of China*

[4]*High Magnetic Field Laboratory, HFIPS, Chinese Academy of Sciences, Hefei 230031, People's Republic of China*

[5]*Collaborative Innovation Centre of Advanced Microstructures, Nanjing University, Nanjing 210093, People's Republic of China*

[6]*Beijing National Laboratory for Condensed Matter Physics, Institute of Physics, Chinese Academy of Sciences, Beijing 100190, People's Republic of China*

(Received 23 September 2023; accepted 5 February 2024; published 7 March 2024)

$PbTaS_2$ is a metal intercalated, layered transition metal dichalcogenide compound which has recently been predicted to be a potential topological superconductor (TSC), with a superconducting transition temperature of 2.6 K. Besides the strong interest in this class of materials, because of their high potential in quantum-computing applications, many aspects of their phenomenology are still undisclosed. Combining angle-resolved photoemission spectroscopy measurements and density functional theory calculations, we have studied the electronic properties of the centrosymmetric type-II superconductor $PbTaS_2$ single crystals in the metallic phase, showing the presence of surface states, originated from the Pb-terminated surface, and of topological nodal lines, formed by the crossing of Ta $d_{xy}/d_{x^2-y^2}$ and Pb p_x/p_y orbitals. The evidence of surface states connecting the nodal lines, as already discovered on structurally similar materials to be typical features of nodal-line semimetal-like TSCs, makes $PbTaS_2$ a good candidate for exploring topological superconductivity.

DOI: 10.1103/PhysRevB.109.125109

I. INTRODUCTION

Topological materials are at the forefront of condensed-matter physics, since they exhibit symmetry-protected metallic edge or surface modes in bulk-insulating or conducting ground states due to a topologically nontrivial ordering of bulk wave functions [1–3]. Within the family of topological materials, topological superconductors (TSCs) attract additional attention because of the zero-energy Majorana bound states present at the superconducting vortex core, which makes this material a suitable candidate for quantum-computing applications [1,2,4–8]. Several works propose that topological superconducting states appear at the interface between a topological insulator and a superconductor [9–13], and recent theoretical studies have also predicted and described that a fully gapped bulk superconductor with topological protected gapless surface states or edge states can be considered in the class of TSCs [14–23].

The type-II superconductor $PbTaSe_2$, which has a noncentrosymmetric structure, has been reported as a TSC [24–30] exhibiting the breaking of spin degeneracy by asymmetric spin-orbit coupling (SOC). The interplay of noncentrosymmetric structure and large SOC has been proposed to be important for nontrivial electronic topological states [31]. Angle-resolved photoemission spectroscopy (ARPES) combined with density functional theory (DFT) calculations has been used to observe and identify, in $PbTaSe_2$, topological surface states (SS), given by the Pb termination of the surface, and nodal lines, caused by the conduction and valence bands crossing in the vicinity of the Fermi level [24,25]. More recently the type-II superconductor $SnTaS_2$, which has a centrosymmetric structure and strong SOC, has been reported to display topological states with SS protected by inversion and time-reversal symmetry and nodal lines near the Fermi energy, making it a good candidate for studying topological superconductivity [32–36]. $PbTaS_2$, which crystallizes in a centrosymmetric structure (similar to $SnTaS_2$) and exhibits strong SOC (as $SnTaS_2$ and $PbTaSe_2$), has been experimentally characterized as a type-II superconductor and predicted to be a TSC [37]. However, the experimental observation of its electronic structure, i.e., SS and nodal lines, has not been reported so far.

In this paper, by combining ARPES measurements and DFT calculations, we describe the presence of SS and nodal lines of $PbTaS_2$ and experimentally observe the existence of SS, originated by the Pb-terminated surface, connecting nodal lines formed by crossing bands of different orbital character.

II. METHODS

The $PbTaS_2$ single crystals used in this work were grown by the chemical vapor transport method [38] with lead chloride as the transport agent following the same procedure

*zhaowj1991@hotmail.com
†wjlu@issp.ac.cn
‡luca.petaccia@elettra.eu

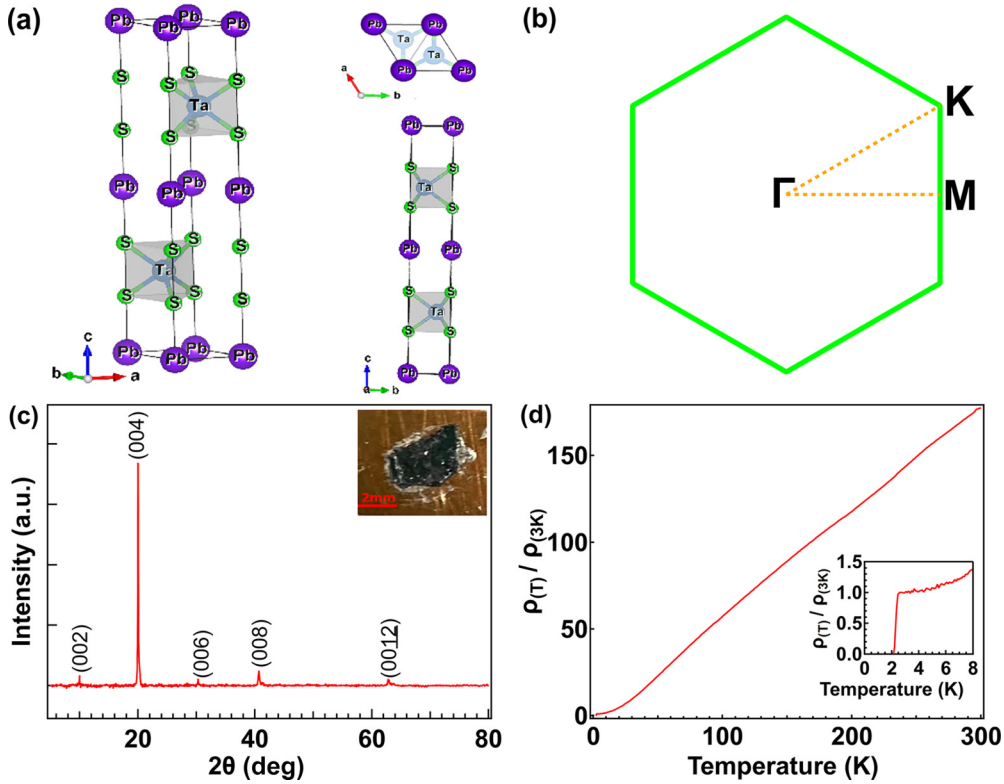

FIG. 1. (a) Cartoonic picture of the $PbTaS_2$ crystal structure with isometric, top, and side views. Purple, blue, and green balls correspond to Pb, Ta, and S atoms, respectively. (b) Surface Brillouin zone with high symmetry points. (c) XRD spectrum of a $PbTaS_2$ single crystal with a sample photograph (inset). (d) Normalized resistivity as a function of temperature measured with current flowing in the *ab* plane. The inset shows the zoom around the superconducting transition temperature.

described by Gao and coauthors [37]. Pb, Ta, and S powders with the mole ratio 1:1:2 were weighted and mixed with $PbCl_2$ and placed into silicon quartz tubes. These tubes were sealed under high vacuum and heated for 10 days in a two-zone furnace, where the temperatures of source and growth zones were fixed at 850 and 800 °C, respectively. As a result, flake crystals were found at the cold end. By means of energy dispersive x-ray, the actual atomic ratio in the single crystals was found to be 0.85:1:1.96. $PbTaS_2$ is known to crystallize in the space group $P6_3/mmc$ [39]. Single-crystal x-ray diffraction (XRD) experiments were performed by the PANalytical X'pert diffractometer using Cu $K_{\alpha 1}$ radiation ($\lambda = 0.154\,06$ nm) at room temperature. Electrical transport measurements were carried out in a Quantum Design Physical Property Measurement System.

The ARPES measurements were performed at the BaDElPh beamline of the Elettra Synchrotron in Trieste [40]. $PbTaS_2$ single crystals were cleaved in ultrahigh vacuum (better than 2×10^{-10} mbar) at room temperature. ARPES data were acquired using horizontal polarized light with the photon energy ranging from 18 to 33 eV. Here, this corresponds to *p*-polarized light as the electrical field vector of the incident light lies in the photoemission plane, which is orthogonal to the sample surface. The spectra were acquired with a SPECS Phoibos 150 electron analyzer. The overall energy and angular resolutions were set at 25 meV and 0.3°, respectively. All measurements were acquired on samples kept at 80 K and under a pressure better than 1×10^{-10} mbar.

The first-principles calculations were based on DFT [41] as implemented in the Vienna *ab initio* simulation package (VASP) [42,43]. The exchange-correlation function is described using the generalized gradient approximation [44] of the Perdew-Burke-Ernzerhof type. The plane-wave cutoff energy was set to 500 eV in all calculations. The structure was fully optimized until the total energy converged to 10^{-6} eV. The Brillouin zone (BZ) was sampled with $18 \times 18 \times 6$ Γ-centered k mesh in all calculations with/without SOC. Wannier functions are constructed by projecting Bloch states onto the *d* orbitals of the Ta atom and the *p* orbitals of the Pb and S atoms through WANNIER90 code [45]. The SS were computed with the WANNIERTOOLS package [46].

III. RESULTS AND DISCUSSION

Figure 1(a) illustrates the layered hexagonal structure of $PbTaS_2$ single crystal formed by the alternating stacks of TaS_2 and Pb layers with the lattice parameters of $a = b = 3.3$ Å and $c = 17.7$ Å [39]. The lattice can also be viewed as a Pb layer intercalated into two adjacent layers of TaS_2, where Ta atoms are located at unequal positions. The corresponding surface BZ is shown in Fig. 1(b) where Γ, K, and M are the high symmetry points.

XRD and resistivity measurements acquired on the $PbTaS_2$ single crystal are shown in Figs. 1(c) and 1(d), respectively. The x-ray diffractogram is characterized by the presence of

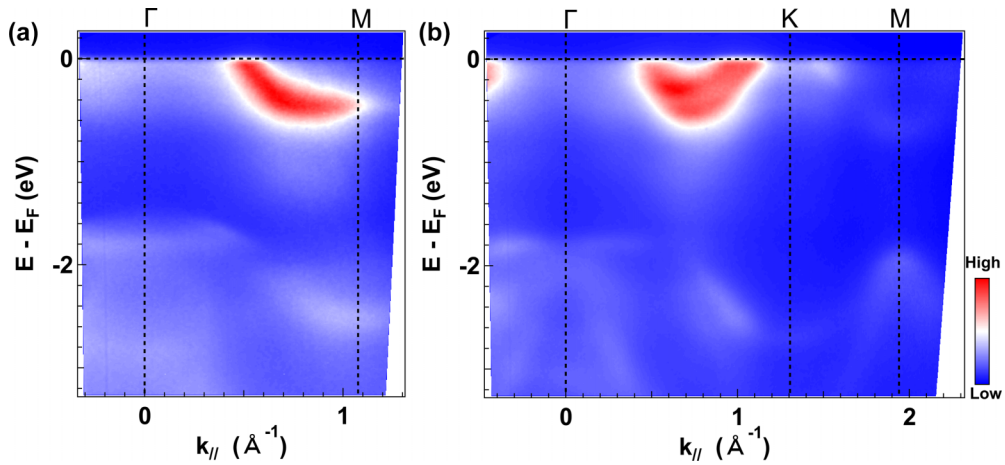

FIG. 2. ARPES band dispersion of $PbTaS_2$ measured with 31 eV photon energy and *p* polarization at 80 K along Γ-M (a) and Γ-K-M (b) directions of the surface BZ.

sharp peaks (00l), with a high signal-to-noise ratio, corresponding to the preferred orientation planes of $PbTaS_2$ and conforming to its quasi-two-dimensional layered structure. The typical single crystal has a large $4 \times 4 \times 0.5$ mm^3 size with a mirrorlike surface. Figure 1(d) displays the normalized resistivity $\rho_{(T)}/\rho_{(3\,K)}$ of $PbTaS_2$ single crystals measured from 300 to 2 K with current applied in the *ab* plane. The overall variation, which is typical of a metallic behavior with a large residual resistivity ratio, and the steep drop in the resistivity curve at $T_c \sim 2.6$ K [inset of Fig. 1(d)] agree with the superconducting phase transition. All these results confirm the good quality of our sample [37].

To address the electronic structure of the freshly cleaved $PbTaS_2$ crystal, we performed ARPES measurements along the high symmetry directions and the results are shown in Fig. 2. The overviews of experimental band structures measured along Γ-M and Γ-K-M with a photon energy of 31 eV in *p* polarization are presented in Figs. 2(a) and 2(b), respectively. In Fig. 2(a) the most intense feature is a hole-type band crossing the Fermi level (FL) at ∼0.49 $Å^{-1}$. At the energy of ~ -0.47 eV, this band gradually becomes flat. At lower energies, a flat band (at ~ -1.8 eV) from the Γ point to ∼0.5 $Å^{-1}$ is present with an adjacent parabolic dispersive band extending to the M point (at ~ -2.6 eV) and some other weaker intensity bands at lower energies. Along Γ-K-M, the ARPES map shown in Fig. 2(b) allows us to identify two intense parabolic (electronlike) bands crossing the FL both at ∼0.47 $Å^{-1}$ and then at 0.94 and 1.08 $Å^{-1}$, respectively. In addition, a parabolic band along the K-M direction of the second BZ crosses the FL at ∼1.47 $Å^{-1}$ and reaches an energy of ~ -0.7 eV at the M point. At lower energies, multiple holelike parabolic bands are detected in the vicinity of the Γ and M points at ~ -1.8 and ~ -2 eV. An intense feature is also visible at ∼0.8 $Å^{-1}$ dispersing from −2 to −2.8 eV towards K. Focusing on the energy region closer to the Fermi level, we investigated the nature of the electronic states to distinguish SS from bulk-derived features, by performing photon energy-dependent ARPES measurements. Since a SS has no dispersion as a function of the out-of-plane momentum, which instead changes with the photon energy, SS features appear at constant energies and parallel momentum in the photon-energy-dependent ARPES data. In Fig. 3(a) the maps measured with photon energy in the range of 21–33 eV are shown to visualize the characteristic electronic structure along the Γ-M direction. The almost linearly dispersive band starting from ~ -0.5 eV and crossing the FL at ∼0.49 $Å^{-1}$ does not change with the photon energy (see Fig. S1 in the Supplemental Material [47]); thus it is compatible with a SS band (SS1) or a bulk state with no dispersion along k_z. The corresponding DFT calculations are presented in Fig. 3(b), showing the difference between the bands' projections along the Γ-M direction considering only the bulk states (left plot) and the bulk states plus the contribution of a Pb-terminated surface state (center plot) and an S-terminated surface state (right plot). The corresponding SS are indicated by black lines and purple arrows. The surface states are not isolated but always at the edge of bulk states. However, along Γ-M the surface state of the Pb-surface termination disappears at higher binding energy (>0.5 eV) and momentum (>0.75 $Å^{-1}$) where only bulk bands are present. The experimentally observed dispersion is compatible with the prediction for the Pb-terminated surface states rather than the S-terminated surface states with the bands at higher binding energy (∼0.5 eV) and parallel momentum position (>0.75 $Å^{-1}$), which show a varying dispersion with the photon energy, associated with bulk states. Therefore, the observed behavior of SS1 and its comparison with the theoretical results support SS1 to be the predicted surface states of the Pb-terminated surface.

A parallel analysis has been performed for the experimental ARPES results along the Γ-K-M direction. The whole set of ARPES maps is shown in Fig. 4(a) to visualize the characteristic electronic structure. The two parabolic bands (SS1 and SS2) crossing the FL at momentum positions of ∼0.47 $Å^{-1}$ and then at 0.94 and 1.08 $Å^{-1}$, respectively, are equally dispersing (see Fig. S1 in the Supplemental Material [47] for the detailed momentum distribution curve (MDC) sequence), only with some intensity changes at the different photon energies, and are compatible with the SS calculated for a Pb-terminated surface [center plot of Fig. 4(b)] rather than with the linearly dispersing SS calculated for an S-terminated surface [right plot of Fig. 4(b)].

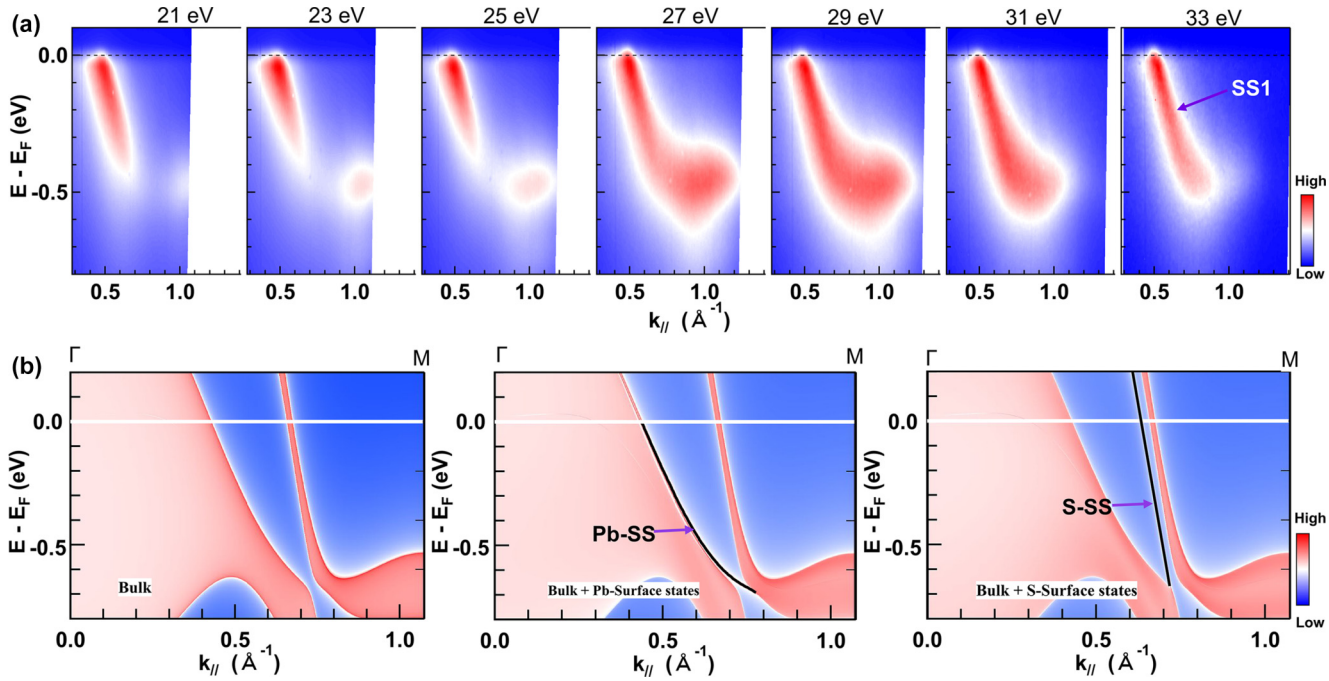

FIG. 3. ARPES maps along the Γ-M [panel (a)] direction showing the SS acquired with photon energy ranging from 21 to 33 eV and a step of 2 eV. The position of the SS (SS1) is marked by a purple arrow in the 33-eV map. DFT + SOC calculated bands from pure bulk, including SS from Pb-terminated or S-terminated surfaces are shown in the left, center, and right plots of panel (b), respectively. The SS are indicated by black lines and marked with purple arrows.

The intensity modulation with photon energies can be explained by a non-negligible contribution of bulk states which mix together with Pb-terminated SS at almost the same positions. Moreover, we show the measured Fermi surface acquired at 31 eV in Fig. S2 in the Supplemental Material [47], which again fits well with that calculated for the Pb-terminated surface. It is worth mentioning that for the inner parabolic band in the Γ-K direction, the measured and calculated dispersions are not perfectly matching, and in particular, the measured lower Fermi momentum has a value

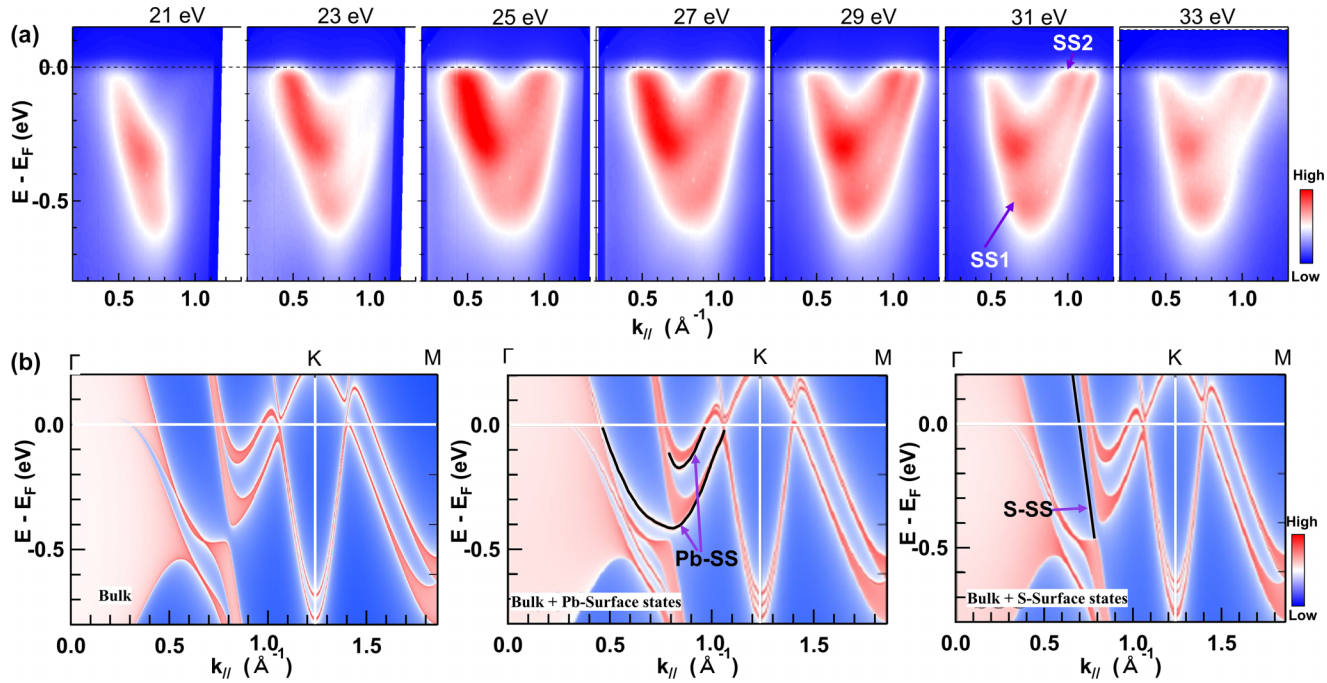

FIG. 4. ARPES maps along the Γ-K-M (a) Direction showing the SS acquired with photon energy ranging from 21 to 33 eV and a step of 2 eV. The positions of the SS (SS1 and SS2) are marked by purple arrows in the 31-eV map. DFT + SOC calculated bands from pure bulk, including SS from Pb-terminated or S-terminated surfaces are shown in the left, center, and right plots of panel (b), respectively. The SS are indicated by black lines and marked with purple arrows.

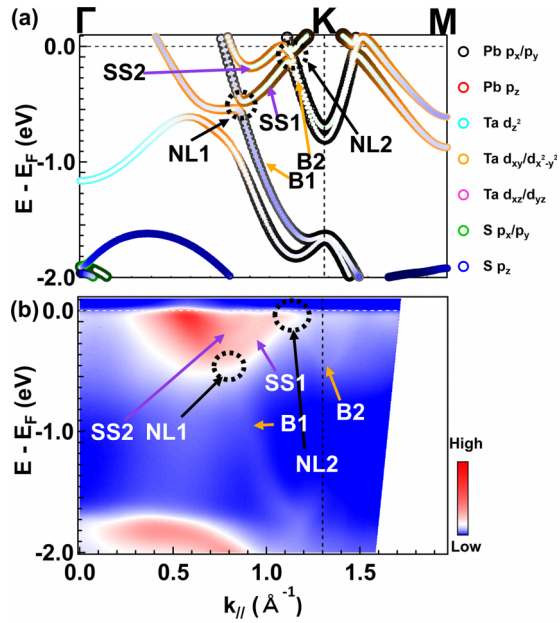

FIG. 5. (a) Orbital band calculations along the Γ-K-M direction. The different orbital components are marked in different colors as summarized in the figure legend. (b) ARPES band dispersion along the Γ-K-M direction and measured with 18 eV photon energy and p polarization at 80 K. Nodal lines (NL1 and NL2) are indicated by black arrows and dashed circles in panels (a) and (b). The SS bands SS1 and SS2 are highlighted by purple arrows while other bands (B1 and B2) around the nodal lines are marked by orange arrows.

of ∼0.2 Å^{-1} smaller than the calculated one. This momentum shift can be due to band renormalization effects caused by defects, like Pb and S atoms vacancies, not considered in the DFT calculations [48,49].

In Fig. 5(a), we report on the calculated bands along the Γ-K-M direction highlighting which orbital brings the major contribution to the bands. In particular, the color scale and the circle size used for the considered orbital are identifying, for each band, the region where that particular orbital becomes predominant and are expected to contribute more to the overall intensity. The two parabolic bands crossing the FL and marked as SS1 and SS2 are mainly contributed by the Ta $d_{xy}/d_{x^2-y^2}$ orbitals with the largest dark orange color circles. The band crossing of the surface state SS1 with the two bands B1 and B2, derived from Pb p_x/p_y orbitals, form two nodal lines, NL1 and NL2, at the positions of ∼0.82 Å^{-1}, −0.5 eV and ∼1.07 Å^{-1}, −0.1 eV, respectively. Since the calculation includes SOC, the nodal lines are all gapped out with gap sizes of 40 and 75 meV for NL1 and NL2, respectively, similar to the typical nodal line gaps reported for $PbTaSe_2$ [24], $SnTaS_2$ [36], and ZrB_2 [50]. Experimentally, SS1 and SS2 are the bands that we identify as Pb-SS (Fig. 4), while B1 and B2 are not revealed with an excitation energy of 31 eV (Fig. 2). By changing the photon energy we have found that the presence of two weak bands, B1 and B2, as shown in Fig. 5(b), is better visible using 18 eV due to the matrix elements effect. One of the two bands (B1) extends from an energy of −0.4 eV at a momentum of 0.82 Å^{-1} to the energy of −1.8 eV at a momentum of 1.16 Å^{-1}. The other one (B2) is an electron-like parabolic band centered at the K point and crossing the Fermi level at ∼1.1 and ∼1.4 Å^{-1}. The experimental band crossings are indicated by black dashed circles in Fig. 5(b). For comparison, we locate NL1 (crossing by B1 and SS1) at a momentum of ∼0.82 Å^{-1} and an energy of −0.4 eV, while NL2 (crossing by SS1 and B2) is located at a momentum of ∼1.07 Å^{-1} close to the FL. This result matches with calculation in Fig. 5(a) with a FL shift of ∼0.1 eV which can be ascribed to crystal defects. Since the Pb-SS band SS1 and the Ta-derived bulk states are overlapping in momentum space, although the SOC gap values cannot be resolved, our results show that the surface band SS1 connects the two nodal line features, thus supporting a topological nontrivial behavior in the electronic structure of $PbTaS_2$.

Concerning the possible relation to topological superconductivity in $PbTaS_2$, bulk topological superconductivity in this system seems unlikely, because the bulk have a center inversion symmetry and non-spin-polarized states, which do not favor the chiral superconducting pairing, e.g., unconventional p-wave symmetry [51]. In addition, bulk measurements have demonstrated $PbTaS_2$ to be a full-gap BCS s-wave superconductor [37], which further denies the possibility of bulk topological superconductivity in this system [51]. The potential topological superconductivity in $PbTaS_2$ is most likely induced on a two-dimensional topological surface state through proximity to a conventional bulk superconductivity [4,8,25,52–54]. In this case, it needs spin-polarized surface states. We have therefore calculated the spin texture of the related surface states in $PbTaS_2$ and the results are shown in Fig. S3 in the Supplemental Material [47]. Our calculations show two spin-momentum-locking Fermi loops of surface states around the Γ point. It is different from the cases of the standard theory model of strong topological insulator [8] and experimental observation of iron-based superconductor $FeTe_{0.55}Se_{0.45}$ [19], which have only one Fermi loop of surface states to be induced into topological superconducting pair. For the two Fermi loops of surface states of $PbTaS_2$, two different topological superconducting pairs could be induced (see schematic diagram in Fig. S3 in the Supplemental Material [47]), which could possibly exhibit characteristics of two superconducting energy gaps. More theoretical and experimental investigations are needed to study the predicated spin-polarized surface states and potential topological superconductivity of $PbTaS_2$ in the future.

IV. CONCLUSION

$PbTaS_2$ is a centrosymmetric superconductor with a transition temperature of 2.6 K and we have investigated by DFT and ARPES its electronic structure along the high symmetry directions of the BZ in its metallic normal phase. By utilizing photon-energy-dependent measurements, we were able to identify two bands with no dispersion along k_z (SS1 and SS2) of the cleaved sample and show they are consistent with the predicted SSs of the Pb-terminated surface. The topological surface states are theoretically predicated to be spin-polarized, which supports the potential topological superconductivity. Previously, a Sn- or Pb-terminated surface has been reported for $SnTaS_2$ [36] and $PbTaSe_2$ [25], respectively. In addition, the measured $PbTaS_2$ electronic structure is compatible with

the presence of nodal lines derived from the crossing of the Pb p_x/p_y orbitals and the Ta $d_{xy}/d_{x^2-y^2}$ orbitals as suggested by first-principles calculations based on DFT including SOC. A surface state connecting two nodal lines is a signature that further supports nontrivial topological properties in $PbTaS_2$ and makes it a good candidate for studying topological superconductivity.

ACKNOWLEDGMENTS

J.G., X.Li., W.L., X.Lu., and Y.S. are thankful for the support from the National Key Research and Development Program of China (Grants No. 2021YFA1600201 and No. 2022YFA1403203) and the National Natural Science Foundation of China (Grants No. U2032215, No. U1932217, and No. 12274412). G.L. acknowledges financial support from the National Key Research and Development Program of China (Grant No. 2022YFA1403901). We thank Luca Sancin for technical assistance during measurements at Elettra.

W.Z., J.G., and X.Li. contributed equally to this work. W.Z., G.L., and L.P. conceptualized the work; W.Z., G.D.S., and L.P. conducted the ARPES experiments and wrote the article with contributions from all coauthors; J.G., X.Lu., and Y.S. prepared the samples and performed the XRD and resistivity measurements; X.Li. and W.L. conducted the DFT calculations; C.S., G.L., and L.P. supported the network. W.Z., W.L., and L.P. are corresponding authors.

[1] M. Z. Hasan and C. L. Kane, *Colloquium:* Topological insulators, Rev. Mod. Phys. **82**, 3045 (2010).

[2] X.-L. Qi and S.-C. Zhang, Topological insulators and superconductors, Rev. Mod. Phys. **83**, 1057 (2011).

[3] M. Zahid Hasan, S.-Y. Xu, and M. Neupane, Topological Insulators, Topological Dirac semimetals, Topological Crystalline Insulators, and Topological Kondo Insulators, in *Topological Insulators* (Wiley-VCH Verlag, Weinheim, Germany, 2015), pp. 55–100.

[4] P. Hosur, P. Ghaemi, R. S. K. Mong, and A. Vishwanath, Majorana modes at the ends of superconductor vortices in doped topological insulators, Phys. Rev. Lett. **107**, 097001 (2011).

[5] C. W. J. Beenakker, Search for Majorana fermions in superconductors, Annu. Rev. Condens. Matter Phys. **4**, 113 (2013).

[6] S. R. Elliott and M. Franz, *Colloquium:* Majorana fermions in nuclear, particle, and solid-state physics, Rev. Mod. Phys. **87**, 137 (2015).

[7] C. W. J. Beenakker, Random-matrix theory of Majorana fermions and topological superconductors, Rev. Mod. Phys. **87**, 1037 (2015).

[8] L. Fu and C. L. Kane, Superconducting proximity effect and Majorana fermions at the surface of a topological insulator, Phys. Rev. Lett. **100**, 096407 (2008).

[9] V. Mourik, K. Zuo, S. M. Frolov, S. R. Plissard, E. P. A. M. Bakkers, and L. P. Kouwenhoven, Signatures of Majorana fermions in hybrid superconductor-semiconductor nanowire devices, Science **336**, 1003 (2012).

[10] M.-X. Wang, C. Liu, J.-P. Xu, F. Yang, L. Miao, M.-Y. Yao, C. L. Gao, C. Shen, X. Ma, X. Chen, Z.-A. Xu, Y. Liu, S.-C. Zhang, D. Qian, J.-F. Jia, and Q.-K. Xue, The coexistence of superconductivity and topological order in the Bi_2Se_3 thin films, Science **336**, 52 (2012).

[11] J.-P. Xu, M.-X. Wang, Z. L. Liu, J.-F. Ge, X. Yang, C. Liu, Z. A. Xu, D. Guan, C. L. Gao, D. Qian, Y. Liu, Q.-H. Wang, F.-C. Zhang, Q.-K. Xue, and J.-F. Jia, Experimental detection of a Majorana mode in the core of a magnetic vortex inside a topological insulator-superconductor, Phys. Rev. Lett. **114**, 017001 (2015).

[12] H.-H. Sun, K.-W. Zhang, L.-H. Hu, C. Li, G.-Y. Wang, H.-Y. Ma, Z.-A. Xu, C.-L. Gao, D.-D. Guan, Y.-Y. Li, C. Liu, D. Qian, Y. Zhou, L. Fu, S.-C. Li, F.-C. Zhang, and J.-F. Jia, Majorana zero mode detected with spin selective Andreev reflection in the vortex of a topological superconductor, Phys. Rev. Lett. **116**, 257003 (2016).

[13] F. Qu, F. Yang, J. Shen, Y. Ding, J. Chen, Z. Ji, G. Liu, J. Fan, X. Jing, C. Yang, and L. Lu, Strong superconducting proximity effect in Pb-Bi_2Te_3 hybrid structures, Sci. Rep. **2**, 339 (2012).

[14] M. Sakano, K. Okawa, M. Kanou, H. Sanjo, T. Okuda, T. Sasagawa, and K. Ishizaka, Topologically protected surface states in a centrosymmetric superconductor β-$PdBi_2$, Nat. Commun. **6**, 8595 (2015).

[15] N. Hao and J. Hu, Topological quantum states of matter in iron-based superconductors: From concept to material realization, Natl. Sci. Rev. **6**, 213 (2019).

[16] S. Sasaki, M. Kriener, K. Segawa, K. Yada, Y. Tanaka, M. Sato, and Y. Ando, Topological superconductivity in $Cu_xBi_2Se_3$, Phys. Rev. Lett. **107**, 217001 (2011).

[17] R. Tao, Y.-J. Yan, X. Liu, Z.-W. Wang, Y. Ando, Q.-H. Wang, T. Zhang, and D.-L. Feng, Direct visualization of the nematic superconductivity in Cu_xBi_2Se, Phys. Rev. X **8**, 041024 (2018).

[18] D. Wang, L. Kong, P. Fan, H. Chen, S. Zhu, W. Liu, L. Cao, Y. Sun, S. Du, J. Schneeloch, R. Zhong, G. Gu, L. Fu, H. Ding, and H.-J. Gao, Evidence for Majorana bound states in an iron-based superconductor, Science **362**, 333 (2018).

[19] P. Zhang, K. Yaji, T. Hashimoto, Y. Ota, T. Kondo, K. Okazaki, Z. Wang, J. Wen, G. D. Gu, H. Ding, and S. Shin, Observation of topological superconductivity on the surface of an iron-based superconductor, Science **360**, 182 (2018).

[20] J.-X. Yin, Z. Wu, J.-H. Wang, Z.-Y. Ye, J. Gong, X.-Y. Hou, L. Shan, A. Li, X.-J. Liang, X.-X. Wu, J. Li, C.-S. Ting, Z.-Q. Wang, J.-P. Hu, P.-H. Hor, H. Ding, and S. H. Pan, Observation of a robust zero-energy bound state in iron-based superconductor Fe(Te,Se), Nat. Phys. **11**, 543 (2015).

[21] Q. Liu, C. Chen, T. Zhang, R. Peng, Y.-J. Yan, C.-H.-P. Wen, X. Lou, Y.-L. Huang, J.-P. Tian, X.-L. Dong, G.-W. Wang, W.-C. Bao, Q.-H. Wang, Z.-P. Yin, Z.-X. Zhao, and D.-L. Feng, Robust and clean Majorana zero mode in the vortex core of high-temperature superconductor $(Li_{0.84}Fe_{0.16})$ OHFeSe, Phys. Rev. X **8**, 041056 (2018).

[22] Y. Fang, J. Pan, D. Zhang, D. Wang, H. T. Hirose, T. Terashima, S. Uji, Y. Yuan, W. Li, Z. Tian, J. Xue, Y. Ma, W. Zhao, Q. Xue, G. Mu, H. Zhang, and F. Huang, Discovery of superconductivity in 2M WS_2 with possible topological surface states, Adv. Mater., **31** 1901942 (2019).

[23] Y. Yuan, J. Pan, X. Wang, Y. Fang, C. Song, L. Wang, K. He, X. Ma, H. Zhang, F. Huang, W. Li, and Q.-K. Xue, Evidence of anisotropic Majorana bound states in 2M-WS_2, Nat. Phys. **15**, 1046 (2019).

[24] G. Bian, T.-R. Chang, R. Sankar, S.-Y. Xu, H. Zheng, T. Neupert, C.-K. Chiu, S.-M. Huang, G. Chang, I. Belopolski, D. S. Sanchez, M. Neupane, N. Alidoust, C. Liu, B. K. Wang, C. C. Lee, H.-T. Jeng, C. Zhang, Z. Yuan, S. Jia *et al.*, Topological nodal-line fermions in spin-orbit metal $PbTaSe_2$, Nat. Commun. **7**, 10556 (2016).

[25] T.-R. Chang, P.-J. Chen, G. Bian, S.-M. Huang, H. Zheng, T. Neupert, R. Sankar, S. Y. Xu, I. Belopolski, G. Chang, B. Wang, F. Chou, A. Bansil, H.-T. Jeng, H. Lin, and M. Z. Hasan, Topological Dirac surface states and superconducting pairing correlations in $PbTaSe_2$, Phys. Rev. B **93**, 245130 (2016).

[26] M. X. Wang, Y. Xu, L. P. He, J. Zhang, X. C. Hong, P. L. Cai, Z. B. Wang, J. K. Dong, and S. Y. Li, Nodeless superconducting gaps in noncentrosymmetric superconductor $PbTaSe_2$ with topological bulk nodal lines, Phys. Rev. B **93**, 020503(R) (2016).

[27] S.-Y. Guan, P.-J. Chen, M.-W. Chu, R. Sankar, F. Chou, H.-T. Jeng, C.-S. Chang, and T.-M. Chuang, Superconducting topological surface states in the noncentrosymmetric bulk superconductor $PbTaSe_2$, Sci. Adv. **2**, 11 (2016).

[28] X. Xu, Z. Kang, T.-R. Chang, H. Lin, G. Bian, Z. Yuan, Z. Qu, J. Zhang, and S. Jia, Quantum oscillations in the noncentrosymmetric superconductor and topological nodal-line semimetal $PbTaSe_2$, Phys. Rev. B **99**, 104516 (2019).

[29] A. Ikeda, M. Kawaguchi, S. Koibuchi, T. Hashimoto, T. Kawakami, S. Yonezawa, M. Sato, and Y. Maeno, Superconductivity in the nonsymmorphic line-nodal compound $CaSb_2$, Phys. Rev. Mater. **4**, 041801(R) (2020).

[30] H. M. Benia, E. Rampi, C. Trainer, C. M. Yim, A. Maldonado, D. C. Peets, A. Stöhr, U. Starke, K. Kern, A. Yaresko, G. Levy, A. Damascelli, C. R. Ast, A. P. Schnyder, and P. Wahl, Observation of Dirac surface states in the noncentrosymmetric superconductor BiPd, Phys. Rev. B **94**, 121407(R) (2016).

[31] M. N. Ali, Q. D. Gibson, T. Klimczuk, and R. J. Cava, Noncentrosymmetric superconductor with a bulk three-dimensional Dirac cone gapped by strong spin-orbit coupling, Phys. Rev. B **89**, 020505(R) (2014).

[32] D.-Y. Chen, Y. Wu, L. Jin, Y. Li, X. Wang, J. X. Duan, J. Han, X. Li, Y.-Z. Long, X. Zhang, D. Chen, and B. Teng, Superconducting properties in a candidate topological nodal line semimetal $SnTaS_2$ with a centrosymmetric crystal structure, Phys. Rev. B **100**, 064516 (2019).

[33] J. Dijkstra, E. A. Broekhuizen, C. F. van Bruggen, C. Haas, R. A. de Groot, and H. P. van der Meulen, Band structure, photoelectron spectroscopy, and transport properties of $SnTaS_2$, Phys. Rev. B **40**, 12111 (1989).

[34] C. Song, L. Liu, S. Cui, J. Gao, P. Song, L. Jin, W. Zhao, Z. Sun, X. Zhang, L. Zhao, X. Luo, Y. Sun, Y. Shi, H. Zhang, G. Liu, and X. J. Zhou, Observation of spin-polarized surface states in the nodal-line semimetal $SnTaS_2$, Phys. Rev. B **107**, 045142 (2023).

[35] K.-H. Jin, H. Huang, J.-W. Mei, Z. Liu, L.-K. Lim, and F. Liu, Topological superconducting phase in high-T_c superconductor MgB_2 with Dirac-nodal-line fermions, npj Comput. Mater. **5**, 57 (2019).

[36] W. Chen, L. Liu, W. Yang, D. Chen, Z. Liu, Y. Huang, T. Zhang, H. Zhang, Z. Liu, and D. W. Shen, Evidence of topological nodal lines and surface states in the centrosymmetric superconductor $SnTaS_2$, Phys. Rev. B **103**, 035133 (2021).

[37] J. J. Gao, J. G. Si, X. Luo, J. Yan, Z. Z. Jiang, W. Wang, C. Q. Xu, X. F. Xu, P. Tong, W. H. Song, X. B. Zhu, W. J. Lu, and Y. P. Sun, Superconducting and topological properties in centrosymmetric $PbTaS_2$ single crystals, J. Phys. Chem. C **124**, 6349 (2020).

[38] A. Ubaldini and E. Giannini, Improved chemical vapor transport growth of transition metal dichalcogenides, J. Cryst. Growth **401**, 878 (2014).

[39] F. J. Di Salvo, G. W. Hull, Jr., L. H. Schwartz, J. M. Voorhoeve, and J. V. Waszczak, Metal intercalation compounds of TaS_2: Preparation and properties, J. Chem. Phys. **59**, 1922 (1973).

[40] L. Petaccia, P. Vilmercati, S. Gorovikov, M. Barnaba, A. Bianco, D. Cocco, C. Masciovecchio, and A. Goldoni, BaD ElPh: A 4 m normal-incidence monochromator beamline at Elettra, Nucl. Instrum. Methods Phys. Res., Sect. A **606**, 780 (2009).

[41] P. Hohenberg and W. Kohn, Inhomogeneous electron gas, Phys. Rev. **136**, B864 (1964).

[42] G. Kresse and J. Hafner, *Ab initio* molecular dynamics for liquid metals, Phys. Rev. B **47**, 558(R) (1993).

[43] G. Kresse and J. Furthmüller, Efficient iterative schemes for *ab initio* total-energy calculations using a plane-wave basis set, Phys. Rev. B **54**, 11169 (1996).

[44] J. P. Perdew, K. Burke, and M. Ernzerhof, Generalized gradient approximation made simple, Phys. Rev. Lett. **77**, 3865 (1996).

[45] A. A. Mostofi, J. R. Yates, G. Pizzi, Y.-S. Lee, I. Souza, D. Vanderbilt, and N. Marzari, An updated version of wannier90: A tool for obtaining maximally-localised Wannier functions, Comput. Phys. Commun. **185**, 2309 (2014).

[46] Q. Wu, S. Zhang, H.-F. Song, M. Troyer, and A. A. Soluyanov, WannierTools: An open-source software package for novel topological materials, Comput. Phys. Commun. **224**, 405 (2018).

[47] See Supplemental Material at http://link.aps.org/supplemental/10.1103/PhysRevB.109.125109 for experimental and theoretical results such as ARPES MDCs vs photon energy, and the comparison between the calculated and measured Fermi surface of the Pb-terminated $PbTaS_2$.

[48] D. O. Scanlon, P. D. C. King, R. P. Singh, A. de la Torre, S. M. K. Walker, G. Balakrishnan, F. Baumberger, and C. R. A. Catlow, Controlling bulk conductivity in topological insulators: Key role of anti-site defects, Adv. Mater. **24**, 2154 (2012).

[49] S. K. Kushwaha, Q. D. Gibson, J. Xiong, I. Pletikosic, A. P. Weber, A. V. Fedorov, N. P. Ong, T. Valla, and R. J. Cava, Comparison of Sn-doped and nonstoichiometric vertical-Bridgman-grown crystals of the topological insulator Bi_2Te_2Se, J. Appl. Phys. **115**, 143708 (2014).

[50] R. Lou, P. Guo, M. Li, Q. Wang, Z. Liu, S. Sun, C. Li, X. Wu, Z. Wang, Z. Sun, D. Shen, Y. Huang, K. Liu, Z.-Y. Lu, H. Lei, H. Ding, and S. Wang, Experimental observation of bulk nodal lines and electronic surface states in ZrB_2, npj Quantum Mater. **3**, 43 (2018).

[51] M. Mandal, N. C. Drucker, P. Siriviboon, T. Nguyen, A. Boonkird, T. N. Lamichhane, R. Okabe, A.

Chotrattanapituk, and M. Li, Topological superconductors from a materials perspective, Chem. Mater. **35**, 6184 (2023).

[52] S.-Y. Guan, P.-J. Chen, and T.-M. Chuang, Topological surface states and superconductivity in non-centrosymmetric $PbTaSe_2$, Jpn. J. Appl. Phys. **60**, SE0803 (2021).

[53] C.-S. Lian, C. Si, and W. Duan, Single anisotropic gap superconductivity and proximity effect in $PbTaSe_2$, Phys. Rev. B **100**, 235420 (2019).

[54] X. Liang, D.-F. Shao, R. Lv, R.-C. Xiao, H.-Y. Lv, W.-J. Lu, and Y.-P. Sun, Ni-intercalation-induced topological nodal line states and superconductivity in NiTe, J. Phys. Chem. C **127**, 4303 (2023).